ECS Transactions

# Application of High-Temperature Raman Spectroscopy (RS) for Studies of Electrochemical Processes in Solid Oxide Fuel Cells (SOFCs) and Functional Properties of their Components

To cite this article: Galina Korableva *et al* 2021 *ECS Trans.* **103** 1301

ECS Transactions, 103 (1) 1301-1317 (2021)
10.1149/10301.1301ecst ©The Electrochemical Society

# Application of High-temperature Raman Spectroscopy (RS) for Studies of Electrochemical Processes in Solid Oxide Fuel Cells (SOFCs) and Functional Properties of their Components

G. M. Korableva[a], D. A. Agarkov[a,b], I. N. Burmistrov[a,b], E. E. Lomonova[c], A. A. Maksimov[a], A.V. Samoilov[a,b], A. A. Solovyev[d], I. I. Tartakovskii[a], V. V. Kharton[a], and S. I. Bredikhin[a,b]

[a] Laboratory of Spectroscopy of Defect Structures, Osipyan Institute of Solid State Physics RAS, Chernogolovka, Moscow region 142432, Russia
[b] Laboratory of Fuel Cells, Moscow Institute of Physics and Technology, Dolgoprudny, Moscow region 141701, Russia
[c] Laboratory "Fianit", Prokhorov General Physics Institute of Russian Academy of Sciences, Moscow 119991, Russia
[d] Laboratory of Applied Electronics, Institute of High Current Electronics SB RAS, Tomsk 634055, Russia

Combined technique and setup have been created that combines capabilities of electrochemical methods, as well as high-temperature Raman spectroscopy (RS) at Osipyan Institute of Solid State Physics RAS. In order to study the processes in the electrochemically active zone, a special geometry of samples was developed on basis of optically transparent single crystal membranes of an anionic conductor with a toroidal shape counter-electrode. With the use of this combined technique and special geometry, studies of the kinetics of reduction of nickel in composite SOFC anodes were carried out. The influence of the composition of fuel on Raman spectra obtained from the internal interface in the current load mode was also investigated, and the correlations with the cell voltage were studied. RS is also used to study the structure of single-crystal samples of anionic conductors, including at SOFCs operating temperature. The new combined technique was used to study other components: sealing glasses for SOFCs and optical glasses.

## Introduction

Solid oxide fuel cells give an opportunity to transform chemical energy of hydrogen (1-2) and hydrocarbon (3-4) fuel oxidation to electrical (5) and heat energy (6). SOFC efficiency is record high one in comparison to other power sources (7), especially in the case of hybrid system with gas turbines (8-9). SOFC efficiency dramatically depends on electrode optimization level (10-11). *In-situ* measurements in SOFC conditions help to understand the mechanism of fuel oxidation on anode electrode to conduct a direct optimization of anode sublayer microstructure and content. Traditional structural and element analysis techniques (e.g. SEM, EDX, XRD, XPS and so on) cannot reach this goal because of severe working conditions of solid oxide fuel cells: working temperature from 550 to 850 $^{o}$C (12), high current densities up to 2-3 A/cm$^2$ (13-15), aggressive gas mixtures and separated gas chambers with fuel and oxidation mixtures. Raman spectroscopy is a promising technique for *in-situ* studies of operating SOFC (16-18). This technique is distance one (it gives opportunity to separate spectroscopic equipment of working SOFC chamber), non-invasive (power input of excitation radiation is relatively low, and it does not significantly influences the operating model SOFC), more than 90 years of studies led to a large database of spectra for different materials, including those used in SOFC industry (19-21).

Raman spectroscopy was widely used for the characterization of materials used for SOFC fabrication as well as full operating SOFC – *ex-situ* and *in-situ*. One of the objects studied was the extremely important issue regarding operation of SOFC anode in natural hydrocarbons – sulfur poisoning. Various bulk nickel sulfides and dramatic morphology changes were observed on the Ni surfaces of Ni–YSZ composites after exposure to fuels with $pH_2S/pH_2$= 100 ppm at elevated temperatures using *in-situ* Raman microspectroscopy and several ex-situ characterization techniques in (16). Raman spectroscopy was used to observe in-situ nickel sulfide formation at temperatures up to about 500°C in (22). Carbon deposition in anode on hydrocarbon-fed solid oxide fuel cells is also widely studied by *in-situ* Raman spectroscopy. Direct evidence of preferential coking on the Ni surface with little to no coking YSZ was provided in (23), and the growth of carbon on the Ni surface was successfully monitored over time at high temperature. Besides, this technique provided additional evidence of the roles that water and BaO modification play in coking resistance on the Ni anode, which is useful for further anode design improvement. Significant and reproducible discrepancies in carbon removal rates by $H_2O$, $CO_2$, and $O_2$ were observed in both spectroscopic graphite signatures and simultaneous changes in cell OCV in (24). Raman spectra showed that the deposited carbon at OCV conditions was mainly in graphitic structure (G band) and partially in amorphous structures with aromatic ring (GR) in (25). As the understanding of fuel oxidations mechanisms strongly influences the direction of anode optimization routine, this subject was also studied in detail using the *in-situ* Raman spectroscopy technique. Oxidation of hydrocarbons (methane and simulated biogas) was studied in (26). Ethanol oxidation as promising SOFC fuel was studied in (27).

Despite all advantages of Raman spectroscopy mentioned above, all the research groups are limited by outer boundaries of samples because of low penetration depth of light. In present work we describe the results obtained on model SOFCs with novel geometry based on optically transparent solid electrolyte membrane (single crystalline or ceramic thin film). This optically transparent anion conductor membrane as well as cathode with special shape give an opportunity to pass excitation laser beam and to collect the scattered radiation from the inner interface of fuel electrode and solid electrolyte membrane.

## Experimental Techniques and Samples

### Model SOFC Samples

In this study we used two types of model SOFCs: electrolyte supported and anode supported planar cells. Principal geometries are shown in figure 1.

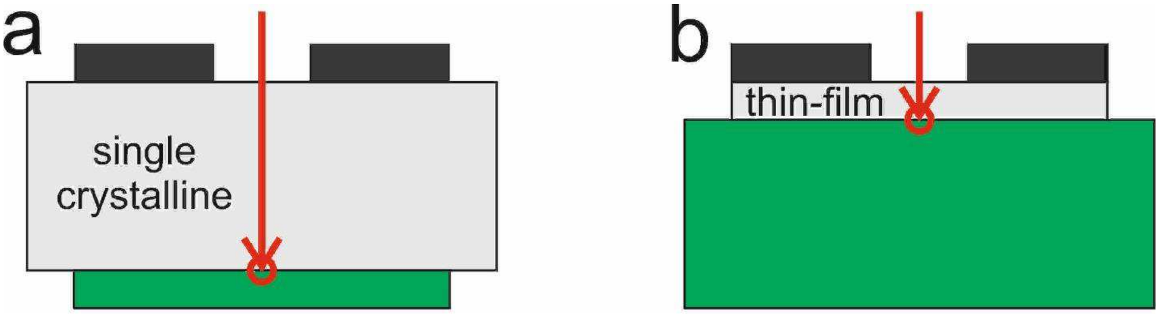

Figure 1. Geometry of electrolyte supported (a) and anode supported planar model SOFCs. Red arrows represent laser beams, red circles – studied zone on the inner interface of solid electrolyte membrane and fuel electrode.

Electrolyte supported cells were used previously (28-32). These samples are based on optically transparent single crystalline membranes made of stabilized zirconia. Despite higher10Sc1YSZ (89 mol% $ZrO_2$ + 10 mol% $Sc_2O_3$ + 1 mol% $Y_2O_3$) ionic conductivity (33-35), we usually used 8YSZ (92 mol% $ZrO_2$ + 8 mol% $Y_2O_3$) material, as it has much simpler Raman spectra (36-37). Single crystalline membranes were cut from the crystals, manufactured in A.M. Prokhorov General Physics Institute RAS (Russia) via direct melt crystallization technique in cold crucible (38-39). Composition and structure optimization of anode and cathode electrodes were described in previous works (40-43). Anode electrode was based on NiO/10Sc1CeSZ (89 mol% $ZrO_2$ + 10 mol% $Sc_2O_3$ + 1 mol% $CeO_2$) composite material, and cathode one – on LSM $(La_{0.8}Sr_{0.2})_{0.95}MnO_{3-d}$/10Sc1CeSZ composite.

Anode supported SOFCs were used to reduce the cell resistance, thus to extend the range of working temperatures and current loads applied. These electrochemical cells were based on thick multilayered anode supports. Thin-film solid electrolyte was deposited using magnetron sputtering in Institute of High Current Electronics SB RAS. Thin-film (3-5 μm) solid electrolyte is also optically transparent due to its low thickness. Cathode electrode was deposited following the route optimized previously (40-43).

In some experiments the 10GDC (90 mol% $CeO_2$ + 10 mol% $Gd_2O_3$) sublayer was placed on the anode | electrolyte boundary due to significant dependence of Raman spectra lines on oxygen stoichiometry in doped ceria crystal lattice (44-45).

### Single-crystal and polycrystalline membrane transparency

Light transmission spectra from (46) for clear (black line) 300 μm thick single-crystal 8YSZ plate and covered by as-prepared thin-film magnetron sputtered 8YSZ-layer for different thicknesses (1.6, 3.0, 4.7 μm) as well as annealed in the air at 1100 °C are shown in figure 2

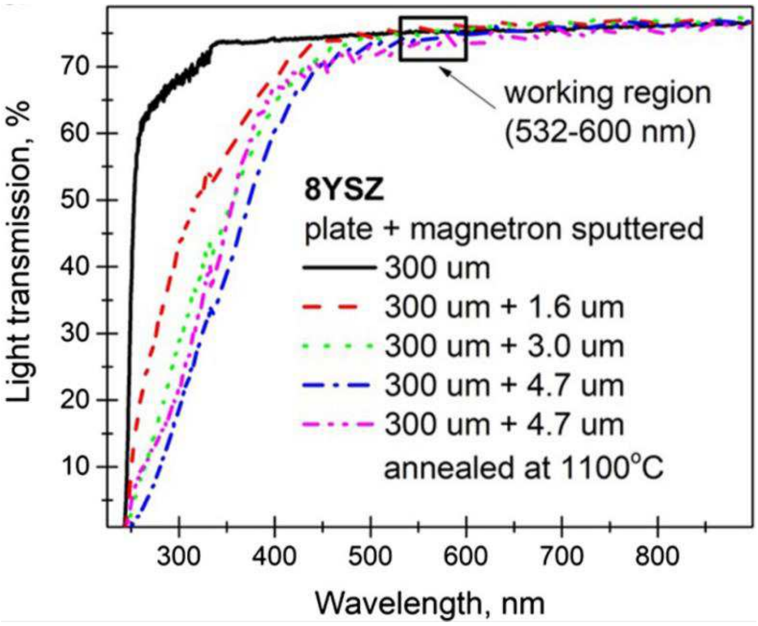

Figure 2. Light transmission spectra of clear (black) 300 μm thick single-crystal 8YSZ plate and covered by as-prepared thin-film magnetron sputtered 8YSZ-layer for different thicknesses (1.6 μm – dashed red, 3.0 μm – dotted green, 4.7 μm – dash-dotted blue) as well as annealed in the air at 1100 °C (4.7 μm – dash-double-dotted magenta), from (46).

One can observe the transmission spectrum of starting 8YSZ single-crystalline plate – black solid line. In a working range of wavelength (indicated with black rectangular) – 532–600 nm – this plate has a transmission ratio on a level of window glass (more than 70%). Introduction of thin-film magnetron sputtered 8YSZ layers (1.6 μm – red dashed line, 3.0 μm – green dotted line, 4.7 μm – blue dash-dotted line) effects the transmission dependence mainly in a shortwave region (200–450 nm), we explain this influence by poor crystallinity of deposited film. Influence of films deposited in working range of wavelength is rather low. Hence, we can use thin-film electrolyte deposited by magnetron sputtering to pass the excitation radiation and get a Raman scattered signal from the inner interface of solid electrolyte and anode electrode. This means, that in combination with special ring-type geometry of cathode electrode with one or several pinholes we have the opportunity to study both electrolyte-supported model SOFC samples based on optically transparent single-crystal solid electrolyte membranes and anode-supported structures with thin-film solid electrolyte deposited by magnetron sputtering technique. This zone and laser beam are represented by red circle and red arrow in figure 1 respectively.

## Experimental Techniques

The morphology of materials as well as microstructure of ceramic layers was studied using a scanning electron microscope (SEM) with a LEO Supra 50VP field emitting cathode.

Thermogravimetric studies were carried out using a Setaram Setsys EVO 16 thermogravimetric analyzer (Setaram, France) with modules of thermogravimetric analysis

(TGA) and differential thermal analysis (DTA) for studies of the temperature dependence of the mass and heat flux, accordingly. The device was equipped with a gas system with consumption controllers allowing to perform measurements in the atmosphere of oxygen, air, argon, technical mixture of argon and hydrogen (4 % hydrogen), carbon dioxide, and also in vacuum.

### Combined Experimental Setup for *in-situ* Raman Studies and Electrochemical Measurements

*In-situ* Raman studies of SOFC electrodes were conducted using combined experimental setup consisting of optical and electrochemical blocks. Principal scheme of this setup is presented in figure 3.

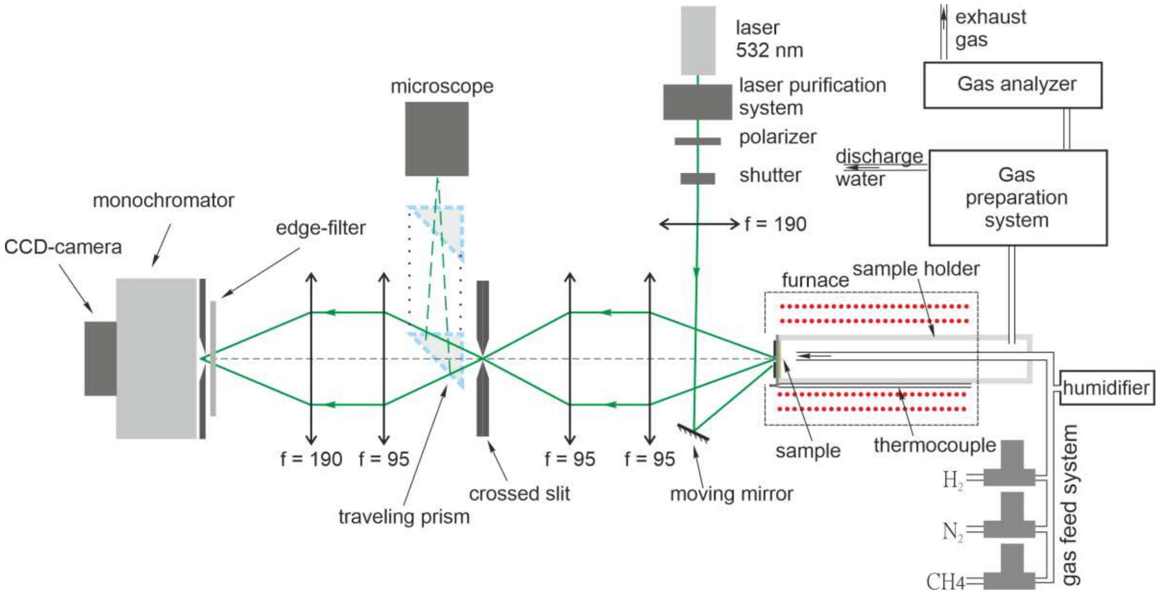

Figure 3. Principal scheme of the combined experimental technique for in-situ Raman studies and electrochemical measurements.

Electrochemical block of combined setup is shown in the right part of the scheme. High-temperature furnace gives an opportunity to control the working temperature of the sample studied up to 1000 °C. High-temperature holder, which is placed inside the furnace, is made of single crystal sapphire tube produced by Osipyan Institute of Solid State Physics RAS (ISSP RAS, Russia). High-temperature holder is fixed on computer controlled mechanical system produced by Avesta-Project (Russia) for precise placing of the sample. Button-shaped SOFC sample is fixed on a tube edge using high-temperature sealing glass. Thermocouples fixed inside and outside of sapphire tube give an opportunity to precisely control the sample working temperature in course of studies. Electrochemical characteristics (chronopotentiometry, current-voltage characteristics, impedance spectroscopy) were measured by potentiostat-galvanostat Gamry Reference 3000 (USA). Gas system based on mass-flow controllers manufactured by Bronkhorst High Tech B.V. (The Netherlands) is connected to hydrogen, nitrogen, CO and $CH_4$ lines, control limit being from 0.25 to 1 l/min for each gas. This system makes it possible to prepare model fuel mixtures for testing model SOFCs in various working conditions. Sample fixed on the edge of sapphire tube is places by one of the edges of high-temperature furnace; this edge is directed towards the setup optical part.

The optical part of the setup consists of excitation radiation sub-system and optical sub-system of the scattered radiation detection. Multimode semiconductor green laser with the wavelength of 532 nm and power output of 20 mW operates as a source of excitation radiation. Spectroscopic filter for 532 nm is used to clear the excitation radiation from different additional lines. Polarizer is used to reduce the radiation intensity in course of system tuning. Mechanical iris-type shutter placed on the trajectory of laser beam is used for the collection of background spectra. Lens with a focus distance of 190 mm focuses laser beam, optical mirror directs it on a model SOFC placed inside the high-temperature furnace. All the lenses in setup described were manufactured by Lytkarino Factory of Optical Glass (LZOS, Russia), they are fixed in precise mechanical shifts for optics manufactured by Avesta-Project (Russia).

Scattered radiation is collected by a pair of lenses with focus distances of 95 mm. The image of the studied area is limited by crossed optical slits to avoid the presence of side signals. Movable prism-type mirror is used to temporarily direct the scattered radiation to microscope with computer-controlled CCD-camera (ToupView, China) with the purpose of precise tuning of investigated region. The second pair of lenses (with focus distances of 95 and 190 mm) directs the scattered radiation through the edge filter on a hole of diffraction grating spectrometer (MDR-12, LOMO, Russia) equipped with nitrogen cooled CCD camera LN/CCD-1340/400-EHRB/1 produced by Roper Scientific (Princeton Instruments, USA) with the size of 1340x400 pixels.

In addition to Raman spectroscopy and traditional electrochemical methods combined experimental setup was equipped with a benchtop flow-through gas analyzer "TEST-1" from Boner-VT, Ltd. (Russia), which makes it possible to study the content of $CO_2$, $CH_4$, $O_2$, CO, $H_2$, and $H_2O$ in the flow gas mixture flowing through the SOFC anode chamber. The use of the flow-through gas analysis system allows dynamic simultaneous measurement of the content of listed gases in the flow of the analyzed gas mixture.

## Results and Discussion

### Studies of SOFC anode fabrication materials

High-temperature Raman spectroscopy allows obtaining additional information on the microstructure of samples both at room and operating temperature, where most other investigation methods become less applicable. Previously it was used to study the structure of single-crystal samples of anionic conductors (47-48), sealing glasses (49-50) for SOFCs, as well as optical glasses (51-53) including in situ experiments at the operating temperature of SOFCs (46).

In-situ Raman spectroscopy was used to study the redox processes at SOFC anode electrode as well as starting materials of anode preparation. Despite the well-known problems such as carbon deposition and Ni coarsening during long-term operation, the anode cermets of metallic Ni and stabilized zirconia are among the most common SOFC materials. Nickel acts as an active component in conventional SOFC anodes (55-56) and takes part in course of fuel oxidation reversibly changing metallic and oxide form. Nickel oxide has complex Raman spectra (58) in contrast to metallic nickel. This property gives the opportunity to follow the redox processes employing nickel oxide Raman spectrum intensity study in course of SOFC operation.

It should be noticed that nickel oxide Raman spectrum is also sensitive to crystalline size (58) but in the case of nano-scale powders with extremely active surface it exhibits no Raman scattering. It was shown (43) that adsorbed layers that cover nanoscale grains could effectively screen laser excitation.

HRTEM revealed a core-shell structure of commercial nickel (II) oxide nanopowder (99.8% purity, Sigma-Aldrich). The amorphous shell, up to 5 nm in thickness, was assumed to be formed by absorbed gaseous species. Indeed, EDX showed a substantially high oxygen hyperstoichiometry of the nanopowder. The amount of extra oxygen decreases on annealing in air and becomes insignificant after heat-treatments at temperatures above 500 °C. The total amount of desorbed oxygen corresponds to 0.18±0.04 atoms per formula unit. The collected Raman spectra of the powders pre-annealed at various temperatures (figure 4) are in excellent agreement with the HRTEM, EDX and TGA data. The first Raman spectrum with well-resolved NiO peaks was collected for the powder annealed at 700 °C, when the absorbates are removed.

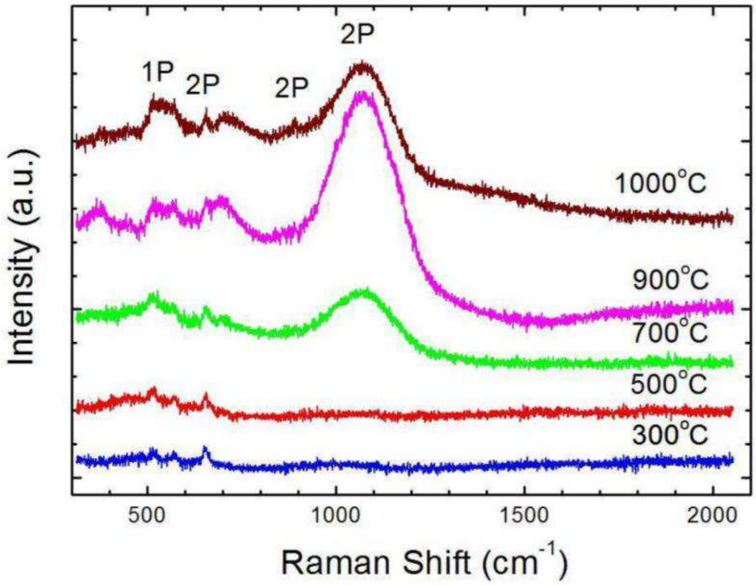

Figure 4. Raman spectra of NiO powders annealed at different temperatures (43).

Studies of nickel oxide reduction kinetics in SOFC working conditions

After solid oxide fuel cell fabrication procedures, nickel oxide is in a form of micro-scale powder with a pronounced Raman spectrum, which can be used to in situ follow the transformation between oxidized and metallic nickel during SOFC anode reduction. The kinetics of reduction of Ni-10Sc1CeSZ composite anodes were studied using the Raman spectroscopy technique (29) for the 400-600 °C temperatures range. Raman spectra of Ni oxide were collected from the region of inner anode | electrolyte interface in the geometry shown in Figure 1 (left). Figure 5 left shows the variation of NiO subspectrum with time during reduction in 50% $H_2$–50% $N_2$ gas mixture at 500 °C. Time dependences of the NiO peak intensity on anode reduction at 400-600 °C are shown in right part of figure 5.

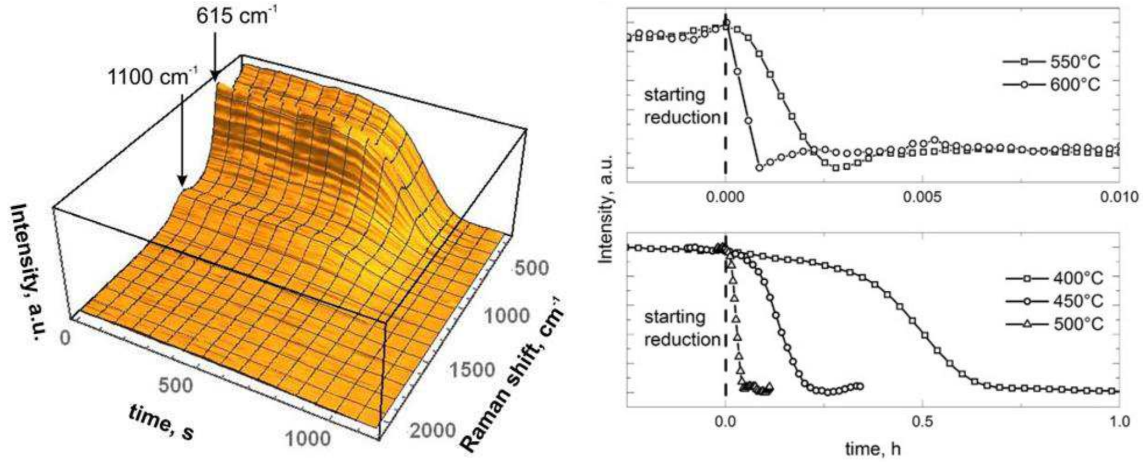

Figure 5. Raman spectra taken from the interface as a function of time during reduction at 500 °C – left, and time dependences of the NiO peak intensity on anode reduction at different temperatures (from (32)).

The time dependence of anode reduction obtained by thermogravimetric analysis of composite powder shows a significant difference from spectroscopic one and can be explained by geometry of Raman measurements as well as penetration depth of excitation laser radiation. Nevertheless, the classical Avrami model can describe both data sets. After initial variation in spectroscopic and thermogravimetric data concerning different experiment geometry both dependences show linear region corresponds to the *n* value of 1.33±0.01, which is in excellent agreement with literature (59-60). The relevant mechanism may be associated with the metal nuclei growth limited by Ni diffusion (60-61). Therefore, under open-circuit conditions the kinetics of NiO reduction at the porous cermet anode | solid electrolyte interface is similar to that of the bulk reaction, as expected. The results on the kinetics of nickel oxide reduction studies within SOFC composite anodes can be used for the optimization of the mode of initial reduction of the anodic electrode when the model medium–temperature SOFC reaches the operating conditions.

### Raman studies of model SOFC samples

Despite high sensitivity of Raman spectroscopy to Ni oxidizing we did not observe any presence of NiO on anode | electrolyte inner interface under current load. To overcome this difficulty, we modified model sample structure by introducing of special indicative layer, sensitive to the oxygen partial pressure and current load applied to the cell. It is well known that cerium oxide has spectral lines, which strongly depend on oxygen stoichiometry in a crystal lattice. That is the reason we used indicative gadolinia doped ceria (GDC) layers in following works (32).

*In-situ* studies of the inner interface between anode electrode and solid electrolyte require optical transparency of this anion conductor membrane. Unlike single crystal conventional ceramic membrane is not optically transparent because of high density of grain boundaries, which significantly scatter light. In the case of thin-films (up to 3-5 μm), when the grain size is comparable to electrolyte thickness, transparency of the ceramic solid electrolyte membrane is much higher. Further results were obtained in comparison of SOFC with single crystal electrolyte support and anode support with ceramic thin-film membrane. In both cases an indicative GDC layer on the anode | electrolyte boundary was used.

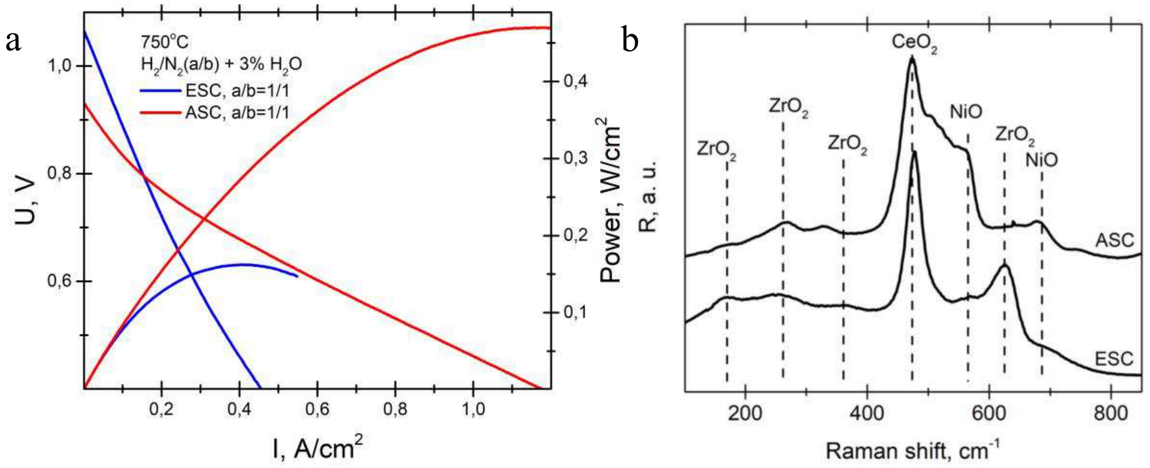

Figure 6. a – current-voltage and current-power curves for the electrolyte- anode supported cells under study at an operating temperature of 750 °C and b – comparison of room temperature spectra for electrolyte- and anode-supported cells with identification of Raman peaks known from literature data.

One can observe from figure 6a, that transition to anode-supported cells gave an opportunity to significantly extend the range of current loads up to 2 A/cm$^2$. It also worth mentioning, that open circuit voltage is rather low, at the level of 0,93-1 V. This issue can be explained by thin-film bilayer electrolyte structure, which can demonstrate micro-leakages in course of SOFC operation. The GDC indicative layer, placed in anode chamber, changes oxidation state of Ce ions in fuel atmosphere. This causes mechanical instability of thin-film electrolyte and may lead to additional leakages, which lower the open circuit voltage of the cell.

Figure 6b shows room temperature Raman spectra obtained from inner interface “anode | electrolyte” of electrolyte-supported (bottom curve) and anode-supported (top curve) model solid oxide fuel cells. The majority of peaks obtained were identified in accordance with Raman spectra of zirconia, ceria and nickel oxide known from the literature data. Raman peaks with shifts of 170, 260, 340, 570 and 610 cm$^{-1}$ can be attributed to the structure of cubic zirconia. These peaks can be explained by the influence of single-crystalline thick solid electrolyte membrane in the case of electrolyte-supported structures and by thin-film polycrystalline 8YSZ membrane deposited by magnetron sputtering in a case of anode supported structures. Despite polycrystalline nature of ASC thin-film electrolyte, an influence of 8YSZ on Raman spectra obtained for ESC structures is much higher due to large thickness of the single-crystalline support membrane. Raman peaks with shifts of 680 and 900 cm$^{-1}$ correspond to nickel oxide present in the functional anode layer. It is quite obvious, that nickel oxide Raman lines are noticeable in a significantly higher degree for anode-supported structure. This result can be explained by two factors: the usage of thin-film solid electrolyte with the lower influence of 8YSZ on total Raman spectrum of ASC sample and higher transparency of GDC layer deposited by means of magnetron sputtering in comparison of screen-printed one in case of thick electrolyte support. Quite intense Raman peak with the shift of about 460 cm$^{-1}$ can be attributed to doped ceria GDC indicative sublayer. Further studies of Raman spectra obtained from the inner interface of the anode electrode and solid electrolyte membrane were carried out in reducing conditions.

The result of the doped ceria line of interest (~460 cm$^{-1}$) separation from Raman spectra for different types of cell and fuel compositions under open circuit conditions is shown in figure 7a.

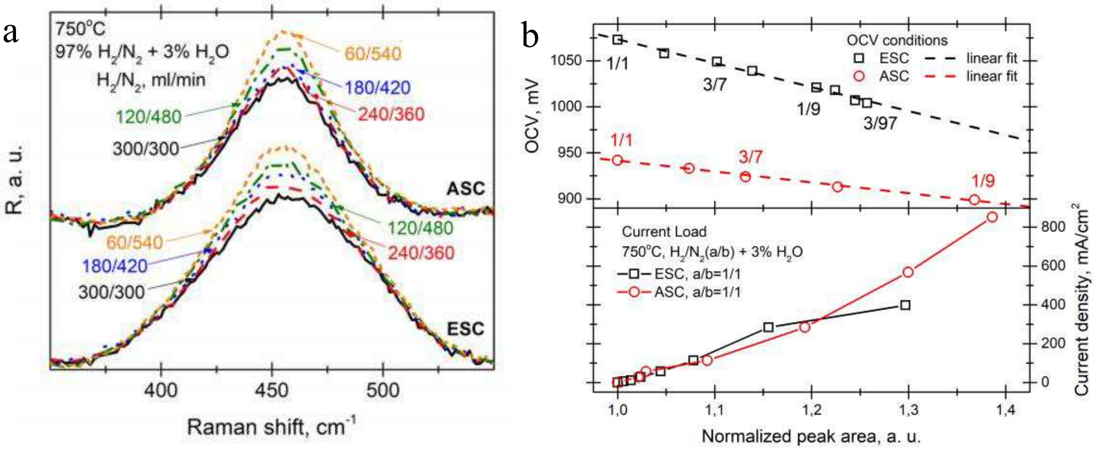

Figure 7. A – result of the doped ceria line of interest (~460 cm$^{-1}$) separation from Raman spectra in dependence on fuel mixture composition (from (46)) and b – dependence of the OCV (top) and current load density (bottom) on normalized Raman peak area.

One can observe a clear dependence of peak intensity on oxygen partial pressure for both types of SOFCs (ECS and ASC): line intensity increases when oxygen partial pressure increases. We connect this change with the growth of oxygen content inside the doped ceria crystal lattice and thus increase of probability of Raman scattering on O-Ce-O lattice oscillations. Dependence with the same character was detected for the case of current load application. Raman peak intensity grew after application of the current load, the higher the current – the higher is peak intensity. This effect can be explained by the transfer of oxygen anion from the electrolyte membrane to the lattice of the indicative GDC sublayer.

Area of the peak was estimated for two types of cells for different fuel compositions at open circuit conditions and for different current loads at constant $H_2/N_2$ ratio. Results of these studies are presented in figure 7b. Peak area was normalized on the line intensity for the case of $H_2/N_2$=1/1 fuel mixture and open circuit conditions.

One can observe that transition to anode-supported structures gives an opportunity to significantly extend the range of current loads available. Maximal current load applied is more than two times higher for the case of anodic support. The general view of the dependence is quite similar for both cell types, it can be attributed to the transport of oxygen anions ($O^{2-}$) from solid electrolyte membrane to anode electrode.

Dependences of OCV on peak area are linear like both for ASC and ESC samples. Assuming local thermodynamical equilibrium on SOFC anode electrode in case of zero currents passing through the cell, one can evaluate a linear connection between changes in 460 $cm^{-1}$ peak area and level of oxygen chemical potential in the region of inner “anode | electrolyte” interface. This procedure was applied to the sets of data obtained at constant fuel gas mixture and various current loads. The result of calculated anode overpotential is presented in figure 8a.

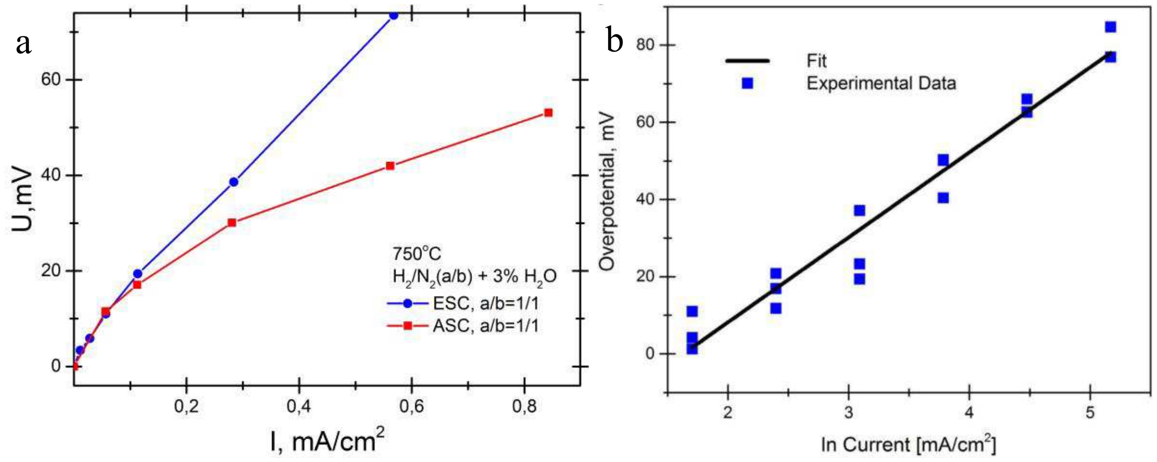

Figure 8. a – Calculated anodic overpotential for electrolyte- and anode-supported model SOFCs, b – Tafel-like dependence of the estimated local overpotential at the GDC|YSZ interface vs. current load for electrolyte-supported SOFC (from (32)).

Type of the supported element has practically no influence on obtained anode overpotential up to the 150 mA/cm$^2$ current load. As was shown earlier for the electrolyte-supported SOFC (32) at low current loads estimated overpotentials exhibit a Tafel-like dependence on the current load applied to the cell (figure 8b). The calculated slope of local overpotential vs. ln(current) dependence equals to RT/(2nF) with $n=2.2 \pm 0.1$. This value was considered close enough to the theoretical value of 2. Moreover, local overpotential at the GDC | YSZ interface depends only on the current density and does not depend on the fuel gas composition within the limits of experimental errors. This fact and a constant slope of the Tafel-like relationship suggest that the rate-limiting mechanism in the reaction zone at low current densities may be associated with anion transfer via this studied interface. For higher current loads overpotential dependence shows a significant difference for different types of cells, which indicates an increase in the role of exchange processes with gaseous phase (e.g. hydrogen oxidation on the GDC surface or in the vicinity of triple-phase boundary).

Studies of carbon deposition in course of SOFC operation in methane-containing fuel

The use of thermodynamic analysis to predict the presence or absence of soot formation in the process of steam conversion of methane does not give an unambiguous answer due to the existence of temperature and concentration gradients between the surface of the fuel cell and the flow in the anode zone, as well as the complex and not fully understood kinetics of steam conversion of methane in general and the kinetics of carbon deposition in particular. However, under such uncertainty, the thermodynamic criterion still gives some confidence in the existence of a regime for reducing or completely preventing carbonization of the fuel cell anode. Therefore, the analysis of the dependence of the concentrations of the components on temperature makes it possible to estimate at what temperature the process of carbon deposition begins, as well as how the limiting concentration of the conversion products changes (for a given input composition). The results of thermodynamic analysis are presented in figure 9.

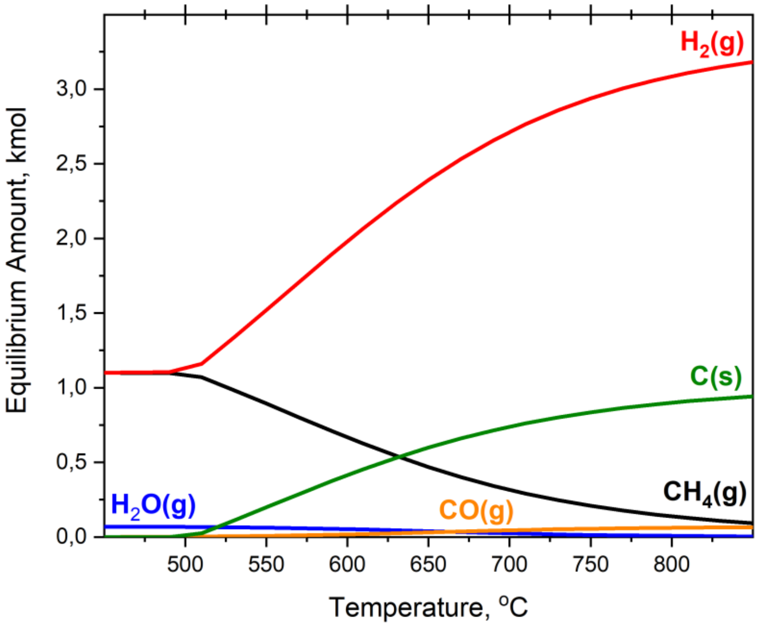

Figure 9. Results of thermodynamic analysis of the process of steam reforming of methane. The total flow of the fuel mixture is 50 ml/min.

As can be seen from figure 9, the addition of methane to the nitrogen-hydrogen mixture should lead to a decrease in the concentration of methane, as well as an increase in the concentration of CO and $H_2$. Carbon deposition can be determined by a significant deviation from the balance between the incoming and outgoing gas mixtures and indirect signs, such as deterioration of the electrochemical characteristics of the fuel cell and an increase in the gas-dynamic resistance of the system.

Standard electrolyte-supported cells based on optically transparent single-crystal solid electrolyte membranes were used in this part of the study. The dominant peak in Raman spectra collected from inner interface of anode and electrolyte is the vibration line in zirconium dioxide due to the passage of the exciting laser beam through the single-crystal membrane of the YSZ anionic conductor and the YSZ content in the composite anode. The Raman spectrum also clearly shows broad vibration lines of nickel oxide (1100 and 1500 cm$^{-1}$), which disappear under operating conditions of SOFC due to the reduction of nickel oxide to metallic nickel.

In order to study the process of carbonization of the composite anode during operation of SOFCs on carbon-containing fuel mixtures, the Raman spectra were measured from the internal interface between the electrolyte and the anode at different compositions of the supplied fuel mixture. Spectra showed that during operation of SOFC on fuel mixture with an increased methane content, a broad line appears in the Raman spectrum at a frequency of 1350 cm$^{-1}$. It is known from the literature that the peak at a frequency of the order of 1360 cm$^{-1}$ corresponds to the so-called D-line of vibrations in disordered graphite (61). It is worth noticing that this line was detected from inner interface of anode and solid electrolyte membrane for the first time. Previous researchers in this direction worked with outer boundaries of model SOFCs (62-63).

It should be noted that this line is wide enough (figure 10 left), which indicates the formation of nanosized "islands" of graphite, which are not strongly interconnected.

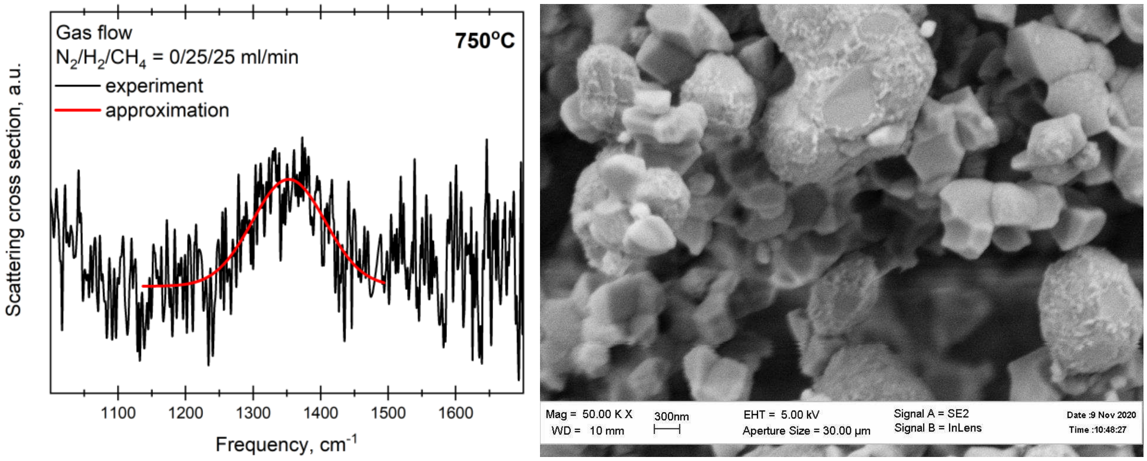

Figure 10. Raman spectrum of the internal interface between the electrolyte and the anode during SOFC operation on a hydrogen-methane mixture in a 1:1 ratio at a temperature of 750 °C.

To confirm that a broad line at a frequency of 1350 cm$^{-1}$ in the Raman spectrum appears as a result of carbonization of the composite anode during operation of SOFCs on carbon-containing fuel (hydrogen-methane mixture), electron microscopic studies of composite anodes of model SOFCs were carried out in this work. The microstructure of the electrode layers of the model SOFC samples was studied using a scanning electron microscope (SEM).

Figure 10 right shows SEM images of the SOFC anode cross section after its operation on methane-hydrogen fuel. It can be seen that after operation on hydrogen-methane fuel, the structure of the anode became more "loose". It can be seen that the surface of the nickel grains is covered with a fine network of carbon deposits. The result obtained confirms the carbonization of the composite cathode, which was detected using the Raman scattering method when operating SOFCs on methane-hydrogen fuel.

We also studied a time dependence of the open circuit voltage (OCV). The reduction of the cell was carried out in a nitrogen-hydrogen fuel mixture with a component ratio of 3:1 ($N_2$:$H_2$ flow). After the completion of the anode reduction and stabilization of OCV at 1060 mV, methane was added to the fuel mixture at the following general ratio of components: $N_2$:$H_2$:$CH_4$ = 3:2:1. From the dependence of the open circuit potential on time, it can be seen that when a new fuel mixture reaches the anode of the fuel cell, a sharp increase in the open circuit potential occurs (1192 mV), which indicates the progress of the methane conversion reaction with the release of hydrogen in the fuel chamber. Moreover, the data of impedance spectroscopy confirm that when methane is added to the fuel gas mixture, the total resistance of the element increases. At the same time, during prolonged exposure in fuel mixtures, the anode structure “loosens” till its gradual destruction, which leads to an excessive increase in resistance, which is confirmed by the data of a scanning electron microscope and impedance. Carbon deposition studies by means of Raman spectroscopy as well as traditional electrochemical techniques will be continued in future works.

## Conclusions

In this manuscript we described results of in-situ measurements of model solid oxide fuel cells conducting using the combined technique, which combines opportunities of Raman spectroscopy and traditional electrochemical techniques. Planar electrolyte- and anode-supported cells were used in these studies. Anode supported cells gave an opportunity to significantly extend ranges of operating temperatures as well as current loads applied. Optical measurements in combination with electrochemical studies gave an opportunity to estimate the dependence of local anodic overpotential on current load applied to the cell. In both cases overpotential exhibits Tafel-like behavior.

Tests of fuel cells under current load have been carried out, the relationship between electrochemical characteristics, composition of reaction products and changes in the corresponding Raman spectra have been studied. It was shown that the addition of methane leads to the formation of CO and an increase in the hydrogen content in the reaction products. In this case, the methane content in the conversion products decreases. It is shown that a more significant decrease in the methane content in relation to the increase in the concentrations of hydrogen and CO can be associated with the Boudouard reaction and carbon deposition. This is confirmed by the fact that over time, the electrochemical characteristics of the fuel cell deteriorate due to carbonization of the SOFC anode when operating in methane-rich mixtures. The influence of hydrocarbon-containing fuel on the evolution of the microstructure and chemical composition of the fuel electrode was studied during model experiments. We found a peak of amorphous carbon in the Raman spectra. It is shown that its occurrence is associated with the deposition of carbon on the model SOFC when using hydrocarbon gas mixtures as fuel.

## Acknowledgments

This work was supported by Russian Scientific Foundation grant 17-79-30071 “Scientifically grounded optimization of power and mass-dimensional characteristics of

planar SOFC stacks and development of fuel processor for highly-efficient transport and stationary power plants".

## References

1. W.G. Bessler, J. Warnatz, and D.G. Goodwin, *Solid State Ionics*, **177**(39-40), 3371 (2007).
2. C.M. Grgicak, R.G. Green, and J.B.Giorgi, *J. Power Sources*, **179**(1), 317 (2008).
3. R.J. Gorte and J.M. Vohs, *J. Catal.*, **216**(1-2), 477 (2003).
4. T. Hibino, A. Hashimoto, M. Yano, M. Suzuki, M. Sano, *Electrochim. Acta*, **48**(17), 2531 (2003).
5. A.B. Stambouli and E. Traversa, *Renew. Sust. Energ. Rev.*, **6**(5), 433 (2002).
6. A.L. Facci, V. Cigolotti, E. Jannelli, and S. Ubertini, *Appl. Energ.*, **192**, 563 (2017).
7. R.A. Raymond, *J. Power Sources.*, **86**(1-2), 134 (2000).
8. A.V. Akkaya, B. Sahin, and H.H. Erdem, *J. Hydrog. Energy*, **33**(10), 2566 (2008).
9. T.W. Song, J.L. Sohn, T.S. Kim, and S.T. Ro, *J. Power Sources*, **158**(1), 361 (2006).
10. D. Ding, X. Li, S.Y. Lai, K. Gerdes, and M. Liu, *Energ. Environment. Sci.*, **7**, 552 (2014).
11. P.R. Shearing, D.J.L. Brett, and N.P. Brandon, *Int. Mater. Rev.*, **55**(6), 347 (2010).
12. P. Charpentier, P. Fragnaud, D.M. Schleich, and E. Gehain, *Solid State Ionics*, **135**(1-4), 373 (2000).
13. A.A. Solovyev, S.V. Rabotkin, A.V. Shipilova, and I.V. Ionov, *Int. J. Electrochem. Sci.*, **14**, 575 (2019).
14. E.A. Smolyanskiy, S.A. Linnik, I.V. Ionov, A.V. Shipilova, V.A. Semenov, A.L. Lauk, and A.A. Solovyev, *J. Phys.: Conf. Ser.*, **1115**, 032080 (2018).
15. A.N. Koval'chuk, A.V. Kuz'min, D.A. Osinkin, A.S. Farlenkov, A.A. Solov'ev, A.V. Shipilova, I.V. Ionov, N.M. Bogdanovich, and S.M. Beresnev, *Russ. J. Electrochem.*, **54**(6), 541 (2018).
16. Z. Cheng and M. Liu, *Solid State Ionics*, **178**(3-4), 925 (2007).
17. M.B. Pomfret, J. Marda, G.S. Jackson, B.W. Eichhorn, A.M. Dean, and R.A. Walker, *J. Phys. Chem. C.*, **112**(13), 5232 (2008).
18. Z. Cheng, J.-H. Wang, Y.M. Choi, L. Yang, M.C. Lin, and M. Liu, *Energ. & Environment. Sci.*, **4**, 4380 (2011).
19. A. Grimaud, J.M. Bassat, F. Mauvy, P. Simon, A. Canizares, B. Rousseau, M. Marrony, and J.C. Grenier, *Solid State Ionics*, **191**(1), 24 (2001).
20. K. Nomura, Y. Mizutani, M. Kawai, Y. Nakamura, and O. Yamamoto, *Solid State Ionics*, **135**, 235 (2000).
21. J.-W. Lee, Z. Liu, L. Yang, H. Abernathy, S.-H. Choi, H.-E. Kim, and M. Liu, *J. Power Sources*, **190**(2), 307 (2009).
22. H.H. Thi, B. Saubat, N. Sergent, and T. Pagnier, *Solid State Ionics*, **272**, 84 (2015).
23. K.S. Blinn, H. Abernathy, X. Li, M. Liu, L.A. Bottomley, and M. Liu, *Energ. & Environment. Sci.*, **5**, 7913 (2012).
24. J. Kirtley, A. Singh, D. Halat, T. Oswell, J.M. Hill, and R.A. Walker, *J. Phys. Chem. C.*, **117**(49), 25908 (2013).
25. W. Li, Y. Shi, Y. Luo, Y. Wang, and N. Cai, *J. Power Sources*, **276**, 26 (2015).
26. J.D. Kirtley, M.B. Pomfret, D.A. Steinhurst, J.C. Owrutsky, and R.A. Walker, *J. Phys. Chem. C.*, 119(23), 12781 (2016).
27. B. Eigenbrodt, J. Kirtley, and R.A. Walker, *ECS Trans.*, **35**(1), 2789 (2011).

28. D.A. Agarkov, I.N. Burmistrov, F.M. Tsybrov, I.I. Tartakovskii, V.V. Kharton, S.I. Bredikhin, and V.V. Kveder, *ECS Trans.*, **68**(1), 2093 (2015).
29. D.A. Agarkov, I.N. Burmistrov, F.M. Tsybrov, I.I. Tartakovskii, V.V. Kharton, and S.I. Bredikhin, *Russ. J. Electrochem.*, **52**(7), 600 (2016).
30. D.A. Agarkov, I.N. Burmistrov, F.M. Tsybrov, I.I. Tartakovskii, V.V. Kharton, and S.I. Bredikhin, *Solid State Ionics*, **302**, 133 (2017).
31. S.I. Bredikhin, D.A. Agarkov, A.S. Aronin, I.N. Burmistrov, D.V. Matveev, and V.V. Kharton, *Mater. Lett.*, **216**, 193 (2018).
32. D.A. Agarkov, I.N. Burmistrov, F.M. Tsybrov, I.I. Tartakovskii, V.V. Kharton, and S.I. Bredikhin, *Solid State Ionics*, **319C**, 125 (2018).
33. D.A. Agarkov, M.A. Borik, S.I. Bredikhin, A.V. Kulebyakin, I.E. Kuritsyna, E.E. Lomonova, F.O. Milovich, V.A. Myzina, V.V. Osiko, E.A. Agarkova, and N.Yu. Tabachkova, *Russ. J. Electrochem.*, **54**(6), 459 (2018).
34. D.A. Agarkov, M.A. Borik, V.T. Bublik, S.I. Bredikhin, A.S. Chislov, A.V. Kulebyakin, I.E. Kuritsyna, E.E. Lomonova, F.O. Milovich, V.A. Myzina, V.V. Osiko, and N.Yu. Tabachkova, *Solid State Ionics*, 322, 24 (2018).
35. F.O. Milovich, M.A. Borik, N.Yu. Tabachkova, D.A. Agarkov, E.E. Lomonova, I.E. Kuritsyna, V.T. Bublik, V.A. Kolotygin, A.S. Chislov, A.V. Kulebyakin, V.A. Myzina, and V.V. Osiko, *J. Alloy Cmpd.*, **191**, 445 (2019).
36. K. Nomura, Y. Mizutani, M. Kawai, Y. Nakamura, and O. Yamamoto, *Solid State Ionics*, **132**(3-4), 235 (2000).
37. I.E. Kuritsyna, S.I. Bredikhin, D.A. Agarkov, M.A. Borik, A.V. Kulebyakin, F.O. Milovich, E.E. Lomonova, V.A. Myzina, and N.Yu. Tabachkova, *Russ. J. Electrochem.*, **54**(6), 481 (2018).
38. M.A. Borik, E.E. Lomonova, V.V. Osiko, V.A. Panov, O.E. Porodnikov, M.A. Vishnyakova, Yu.K. Voron'ko, and V.V. Voronov, *J. Cryst. Growth*, **275**, e2173 (2005).
39. V.I. Aleksandrov, V.V. Osiko, A.M. Prokhorov, and V.M. Tatarintsev, *Russ. Chem. Rev.*, **47**(3), 213 (1978).
40. I. Burmistrov, D. Agarkov, S. Bredikhin, Yu. Nepochatov, O. Tiunova, and O. Zadorozhnaya, *ECS Trans.*, **57**(1), 917 (2013).
41. I.N. Burmistrov, D.A. Agarkov, F.M. Tsybrov, and S.I. Bredikhin, *Russ. J. Electrochem.*, **52**(7), 669 (2016).
42. I.N. Burmistrov, D.A. Agarkov, E.V. Korovkin, D.V. Yalovenko, and S.I. Bredikhin, *Russ. J. Electrochem.*, **53**(8), 873 (2017).
43. I.N. Burmistrov, D.A. Agarkov, I.I. Tartakovskii, V.V. Kharton, and S.I. Bredikhin, *ECS Trans.*, **68**(1), 1265 (2015).
44. J.R. McBride, K.C. Hass, B.D. Poindexter, and W.H., *J. Appl. Phys.*, **76**, 2435 (1995).
45. W.H. Weber, K.C. Haas, and J.R. McBride, *Phys. Rev. B.*, **48**(1), 178 (1993).
46. D.A. Agarkov, I.N. Burmistrov, G.M. Eliseeva, I.V. Ionov, S.V. Rabotkin, V.A. Semenov, A.A. Solovyev, I.I. Tartakovskii, and S.I. Bredikhin, *Solid State Ionics*, **344,** 115091 (2020).
47. D.A. Agarkov, M.A. Borik, S.I. Bredikhin, I.N. Burmistrov, G.M. Eliseeva, A.V. Kulebyakin, I.E. Kuritsyna, E.E. Lomonova, F.O. Milovich, V.A. Myzina, and N.Yu. Tabachkova, *Solid State Ionics*, **346**, 115218 (2020).
48. D.A. Agarkov, M.A. Borik, S.I. Bredihin, V.T. Bublik, L.D. Iskhakova, A.V. Kulebyakin, I.E. Kuritsyna, E.E. Lomonova, F.O. Milovich, V.A. Myzina, S.V. Seryakov, and N.Yu. Tabachkova, *Russ. Microelectron.*, **45**(8-9), 625 (2016).A.

Allu, S. Balaji, D. Tulyaganov, G. Mather, F. Margit, M. Pascual, R. Siegel, W. Milius, J. Senker, D. Agarkov, V. Kharton, and J. Ferreira, *ACS Omega*, **2**, 6233 (2017).

49. A. Allu, A. Gaddam, S. Ganisetti, S. Balaji, R. Siegel, G. Mather, M. Fabian, M. Pascual, N. Ditaranto, W. Milius, J. Senker, D. Agarkov, V. Kharton, and J. Ferreira, *J. Phys. Chem. B.*, **22**(17), 4737 (2018).
50. M.K. Kokila, P. Ramesh, Vinod Hegde, A.G. Pramod, B. Eraiah, R.S. Venugopal, S. Shisina, D. Subrata, D.A. Agarkov, G.M. Eliseeva, and G. Jagannath, *Opt. Mater*., **108**, 110051 (2020).
51. M.K. Kokila, P. Ramesh, V. Hegde, A.G. Pramod, B. Eraiah, D.A. Agarkov, G.M. Eliseeva, M.K. Pandey, K. Annapurna, and G. Jagannath, *Solid State Sci.*, **107**, 106360 (2020).
52. P. Ramesh, J. Gangareddy, K.N. Sathish, A.G. Pramod, V. Hegde, U. Mahaboob Pasha, S. Khan, K. Annapurna, M.I. Sayyed, A.M.S. Alhuthali, D.A. Agarkov, and M.K. Kokila, *Opt. Mater.*, **114**, 110933 (2021).
53. T. Fukui, S. Ohara, M. Naito, and K. Nogi, *J. Power Sources*, **110**(1), 91 (2002).
54. T. Fukui, K. Murata, S. Ohara, H. Abe, M. Naito, and K. Nogi, *J. Power Sources*, **125**(1), 17 (2004).
55. D. Sarantaridis and A. Atkinson, *Fuel Cells*, **7**(3), 246 (2007).
56. N. Mironova-Ulmane, A. Kuzmin, I. Steins, J. Grabis, I. Sildos, and M. Pärs, *J. Phys.: Conf. Ser.*, **93**(1), 012039 (2007).
57. A.F Benton and P.H. Emmett, *J. Am. Chem. Soc.*, **46**(12), 2728 (1924).
58. J.T. Richardson, R. Scates, and M.V. Twigg, *Appl. Catal. A. Gen.*, **246**(1), 137 (2003).
59. S.F. Hulbert, *J. Brit. Ceram. Soc.*, **6**, 11 (1969).
60. M.J. Matthews, M.A. Pimenta, G. Dresselhaus, M.S. Dresselhaus, and M. Endo, *Phys. Rev. B*, **59**, R6585(R) (1999).
61. X. Li, M. Liu, J. Lee, D. Ding, L.A. Bottomley, S. Park, and M. Liu, *Phys. Chem. Chem. Phys.*,17, 21112 (2015).
62. R.C. Maher, V. Duboviks, G.J. Offer, M. Kishimoto, N.P. Brandon, and L.F. Cohen, *Fuel Cells*, **13**(4), 455 (2013).
63. J. Kirtley, A. Singh, D. Halat, T. Oswell, J.M. Hill, and R.A. Walker, *Phys. Chem. C*, **117**(49), 25908 (2013).